

Local Jet Pattern: A Robust Descriptor for Texture Classification

Swalpa Kumar Roy[†], Bhabatosh Chanda, Bidyut B. Chaudhuri, Dipak Kumar Ghosh and Shiv Ram Dubey

Abstract—Methods based on locally encoded image features have recently become popular for texture classification tasks, particularly in the existence of large intra-class variation due to changes in illumination, scale, and viewpoint. Inspired by the theories of image structure analysis, this work proposes an efficient, simple, yet robust descriptor namely local jet pattern (LJP) for texture classification. In this approach, a jet space representation of a texture image is computed from a set of derivatives of Gaussian (DtGs) filter responses up to second order, so-called local jet vectors (LJV), which also satisfy the Scale Space properties. The LJP is obtained by using the relation of center pixel with its' local neighborhoods in jet space. Finally, the feature vector of a texture image is formed by concatenating the histogram of LJP for all elements of LJV. All DtGs responses up to second order together preserves the intrinsic local image structure, and achieves invariance to scale, rotation, and reflection. This allows us to design a discriminative and robust framework for texture classification. Extensive experiments on five standard texture image databases, employing nearest subspace classifier (NSC), the proposed descriptor achieves 100%, 99.92%, 99.75%, 99.16%, and 99.65% accuracy for Outex_TC10, Outex_TC12, KTH-TIPS, Brodatz, CURET, respectively, which are better compared to state-of-the-art methods.

Index Terms—Derivative-of-Gaussian (DtGs) Jet space Local jet vector (LJV) Local jet Pattern (LJP) Texture classification.

I. INTRODUCTION

Computer vision and pattern classification areas have seen enormous progress in the last five decades, having several potential applications such as multimedia event detection [5], texture recognition [22], [45], motion detection [4], event analysis [6], face and head pose recognition [33], image retrieval [71], mobile landmark search [72], mobile and multimedia retrieval [61], [73] etc. Since texture is a repeated basic primitives visual pattern that describes the distinctive appearance of many natural objects and is present almost everywhere, it shows a useful role in the areas of computer vision and pattern classifications namely object recognition, natural scene identification, material classification, and image

segmentation [16], [53], [62]. A crucial issue of texture classification is efficient texture representation, which can be categorized into geometrical, statistical, structural, signal processing based, and model-based methods [18], [24], [47]. A picture may be captured under various geometric and photometric varying conditions, and hence an ideal texture model for texture classification should be robust enough against the changes in illuminance, view-point, rotation or reflection, scale, and geometry of the underlying surface. Earlier texture classification methods mainly concentrated on the statistical analysis of texture images. In recent literature, two categories of texture classification approaches dominate current research, namely texture descriptor based methods [22], [43], [46] and deep learning based methods [1], [9], [10], [30], [37]. In deep learning based methods a Convolutional Neural Network (CNN) has been proposed and trained to classify the texture images [3], [9]. The deep learning based methods offer good classification performance, however, it has the following limitations: it requires a large amount of data and it is computationally expensive to train. The complex models take weeks to train sometimes using several machines equipped with expensive GPUs. Also, at present, no strong theoretical foundation of finding the topology/training method/ flavor/hyper-parameters for deep learning exist in the literature. On the other hand, the descriptor based methods have the advantage of easy to use, data independence, and robustness to real-life challenges such as illumination and scale differences. Therefore, attention is given here to form the local texture descriptors which are adequate for achieving local invariance [11], [55], [56], [67], [70].

The search for invariances started in the nineties of last century [59]. In the beginning, a circular autoregressive dense model has been proposed by Kashyap and Khotanzad to study the rotation invariant texture classification [28]. To study rotation invariance texture classification, many other models were explored such as hidden Markov model [8], multi-resolution [40], Gaussian Markov model [13], etc. Currently, Varma and Zisserman introduced a texton dictionary-based method for rotation invariant texture classification [55]. Later on, they also proposed another texton based method where the features are directly represented utilizing the image local patch [56]. Recently, some works are also introduced scale and affine invariant feature extraction for texture classification. Chaudhuri and Sarkar proposed a technique for texture recognition based on differential box-counting (DBC) [7] based algorithm. Varma and Garg [54] extracted a local fractal vector for each pixel, and computed a statistical histogram; Liu and Fieguth [36] applied random projection for densely

S. K. Roy and B. Chanda are with the Electronics and Communication Sciences Unit at Indian Statistical Institute, Kolkata 700108, India (email: swalpa@ieee.org; chanda@isical.ac.in).

B. B. Chaudhuri is with the Computer Vision and Pattern Recognition Unit at Indian Statistical Institute, Kolkata 700108, India (email: bbc@isical.ac.in).

D. K. Ghosh is with the Department of Electronics & Communication Engineering at National Institute of Technology, Rourkela, Orissa 769008, India (email: dipak@ieee.org).

S. R. Dubey is with the Computer Vision Group at Indian Institute of Information Technology, Sri City, Andhra Pradesh-517646, India (email: srdubey@iiits.in).

* Corresponding author email: swalpa@students.iiests.ac.in, swalpa@ieee.org.

sampled image patches, and extracted the histogram signature; Yao and Sun [65] normalized statistical edge feature distribution to resist variation in scale; Lazebnik *et al.* [31] and Zhang *et al.* [70] detected Harris and Laplacian regions and extracted texture signatures after normalizing these regions. Recently, global scale invariant feature extraction methods drew attention because local scale normalization is usually slow due to pixel by pixel operations. Xu *et al.* [64] and Quan *et al.* [46] have classified the image pixels into multiple point sets by gray intensities or local feature descriptors. Other than extracting scale invariant features, pyramid histograms with shifting matching [11] scheme were also proposed by some researchers [69]. In order to impart more robustness, feature extraction is often performed locally. In 1996 a computationally efficient texture descriptor, called local binary pattern (LBP) was proposed by Ojala *et al.* [44], [45] for gray-scale and rotation invariant texture classification. Later on, other variants of LBP such as center-symmetric LBP (CSLBP) [26], derivative-based LBP [68], LBP variance (LBPV) [23], the dominant LBP (DLBP) [34], the completed model of LBP (CLBP) [22], order-based local descriptor [14], local wavelet pattern [15], multichannel decoded LBP [17], Complete Dual-Cross Pattern (CDCP) [50], Local ZigZag Pattern (LZP) [49], and Local Morphological Pattern (LMP) [51] etc. were introduced in numerous applications of computer vision and pattern recognition. But these methods could not address the scaling issue very well and LBP feature alone could not achieve good performance. However, the feature values of a texture image vary with the scale, it is difficult to know if a query texture image has the same scale as the target images. Recently, Quan *et al.* [46] proposed a multi-scale LBP based global fractal feature to solve the scale issue. But this feature is not robust for small sized images. Li *et al.* [32] proposed a technique to find the optimal scale for each pixel and extracted LBP feature with the optimal scale. However, it failed to extract accurate and consistent scale for all pixels. To extract scale invariant feature, Guo *et al.* [21] proposed scale selective complete local binary pattern-(SSCLBP). Although their reported results are quite impressive, they did not establish the relation between image structure and scale parameter.

Noise, which introduces additional geometric variation, can also create problems for texture image recognition. Hence, noise tolerant and robust texture recognition problem drew attention of the research communities. Tan and Triggs [52] proposed local ternary pattern (LTP) for noise invariant texture classification. However, LTP is not purely gray-scale invariant. Ren *et al.* [48] introduced a relatively more effective noise resistant local binary pattern (NRLBP) scheme based on LBP, but it is computationally expensive for bigger scales with larger number of neighboring points. Liu *et al.* proposed binary rotation invariant and noise tolerant (BRINT) feature [38]. However, to calculate BRINT, they used a multi-scale approach which is computationally expensive and suffers from high dimensionality problem. To the best of our knowledge, no work is reported in the literature that simultaneously deals with invariance to scale, translation, rotation, or reflection and insensitive to noise of a texture image. To achieve such

invariance properties, it appears that local patterns from a Jet Space [20] of the image may be useful. Based on this assumption, we propose here an effective local jet space descriptor, named as local jet pattern (LJP). To extract the LJP, at first the Jet Space of a texture image is derived by convolving the derivative of Gaussian (DtGs) kernels upto 2^{nd} order. Then, the LJP for each element of Jet Space is built by exploiting the local relationships in that space. Finally, for a texture image, the normalized feature vector is formed by concatenating histogram of LJP for all elements of the Jet Space. The main contributions of this paper can be summarized as follows,

- We propose a simple, effective, yet robust jet space based texture descriptor called local jet pattern (Sec. III) for texture classification. In the jet space, the properties of Hermite polynomial are utilized to make DtGs responses for preserving the intrinsic local image structure in a hierarchical way.
- The LJP descriptor achieves sufficient invariance to address the challenges of scale, translation, and rotation (or reflection) for texture classification. In addition, the proposed descriptor is also robust to the variations of noise.
- The proposed algorithm takes very reasonable amount of time in feature extraction.
- We experimented and observed that the proposed descriptor outperforms to the traditional LBP and other state-of-the-art methods on different benchmark texture databases, such as KTH-TIPS and CURET (Sec. IV) etc.

The rest of the paper is organized as follows. Sec. II deals with the mathematical definition of a broad class of local image decomposition's, jet and jet space. The proposed LJP feature extraction scheme is presented in Sec. III. In Sec. IV the performance of texture classification is compared with the state-of-the-art methods. Finally, concluding remarks are drawn in Sec. V.

II. IMAGE STRUCTURE ANALYSIS, JETS AND JET SPACE

Image analysis is an important part of most image processing tasks. As a general framework to deal with image structures at different resolution, the Scale Space representation is introduced in [35]. The idea of "local deep structure" is linked to the concept of derivative: given by

$$I'(0) = \lim_{\Delta \rightarrow 0} \frac{I(0+\Delta) - I(0)}{\Delta}$$

where \mathcal{I} denotes image intensity. This expression is not appropriate to discrete domain, such as images, that are the result of quantized measurement. The scale space analysis [35] introduces a two-step solution for image derivative measurement as follows:

First, a measure of inner scale changing of an image is described, by convolving (denoted by $*$) the image with Gaussian kernels. The 1D Gaussian kernels at scale $\sigma \in \mathbb{R}^+$ are defined as

$$G_{\sigma}(x) = \frac{1}{\sigma\sqrt{2\pi}} \exp\left\{-\frac{x^2}{2\sigma^2}\right\}$$

The convolution of 2- \mathcal{D} Gaussian function with an image patch can be smoothly computed by applying the 1- \mathcal{D} Gaussian function using two passes in the horizontal and vertical directions which exhibits the separable [39] property of 2- \mathcal{D} Gaussian function: $G_\sigma(x, y) = G_\sigma(x)G_\sigma(y)$. The scaling operation to obtain $I_\sigma = G_\sigma * I$ can be computed efficiently and stably due to the space and frequency localization of the Gaussian [57] even if the input image function I is directly sampled and yields the result of physical measurement.

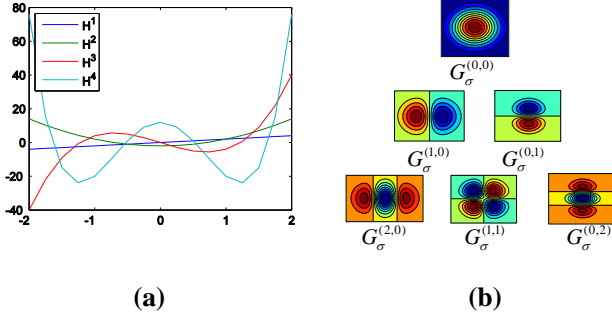


Fig. 1: (a) Hermite polynomial of different orders. (b) The 2- \mathcal{D} derivatives of the Gaussian (DtGs) upto 2nd order.

Secondly, the scale space approach to calculate image derivative of a rescaled image can be done alternatively by convolving the original image with the DtGs ($I_\sigma = G_\sigma * I$) as proposed by Young [66]. He showed that Gaussian derivatives fit more accurately for the measurement of image structure at our receptive fields than other functions such as Gabor function does. The DtGs at scale $\sigma > 0$ is defined in 1- \mathcal{D} by $G_\sigma(x) = G_\sigma^0(x) = \frac{1}{\sigma\sqrt{2\pi}} \exp\left(-\frac{x^2}{2\sigma^2}\right)$.

$$G_\sigma^m(x) = \frac{d^m}{dx^m} G_\sigma(x) = \left(\frac{-1}{\sigma\sqrt{2}}\right)^m \mathbf{H}^m\left(\frac{x}{\sigma\sqrt{2}}\right) G_\sigma(x) \quad m \in \mathbb{Z}^+ \quad (1)$$

where $G_\sigma^0(x)$ is the original Gaussian, m is a positive integer, and $H^m(x)$ is the n^{th} order Hermite polynomial (Fig. 1(a)) [41]. It is also useful to perform normalizations of the DtGs, such that $\int |G_\sigma^k(x)| dx = 1$. In particular, $G_\sigma^0(x)$ and $G_\sigma^1(x)$ are the ℓ^1 -normalized blurring and differentiating filters, respectively. Hermite transform was originally developed for the mathematical modelling of the properties in early stages of (human) vision [41]. From the properties of the Hermite polynomials, one sees that the neighborhood functions for even order are *symmetrical* ($G_\sigma^m(-x) = G_\sigma^m(x)$), whereas these for odd order are *anti-symmetrical* ($G_\sigma^m(-x) = -G_\sigma^m(x)$). For the evaluation of the results of the neighborhood operators (that is, the $G_\sigma^m(x)$) all over an image, it pays to move to the Fourier domain. The Fourier representation of a convolution with the n^{th} order operator becomes a multiplication with an n^{th} power times a Gaussian frequency envelope, which leads to practical implementations. The DtGs at scale $\sigma > 0$ are defined in 2- \mathbb{D} (Fig. 1(b)) by

$$\begin{aligned} G_\sigma^{(m,n)}(x,y) &= G_\sigma^m(x)G_\sigma^n(y), \quad m,n \in \mathbb{Z}^+ \\ G_\sigma^{(0,0)}(x,y) &= G_\sigma^0(x,y) \end{aligned} \quad (2)$$

Thus, the scale-space method allows to compute the image derivatives of any order at any scale. The convolution formalism should be used when derivatives are required throughout the entire image, whereas an inner product formalism ($\langle \cdot | \cdot \rangle$) is more acceptable if derivative at a single location is required. For instance, the image derivatives at scale σ , with respect to the origin is defined as,

$$\begin{aligned} J_{(m,n)} &= (-1)^{(m+n)} \langle G_\sigma^{(m,n)} | I \rangle \\ &= (-1)^{(m+n)} \int_{x,y \in \mathbb{R}} G_\sigma^{(m,n)}(x,y) I(x,y) dx dy. \end{aligned} \quad (3)$$

Note that the image derivative measurements $J_{m,n}$ (Fig. 2) are dependent on the inner scale σ , though we do not indicate it with a superscript to prevent cluttered appearance of the equations. Furthermore, we get scale normalized DtGs response ($J_{(m,n)}^s$) by multiplying σ^{n+m} with the corresponding $J_{(m,n)}$ represented as,

$$J_{(m,n)}^s = \sigma^{n+m} J_{(m,n)}. \quad (4)$$

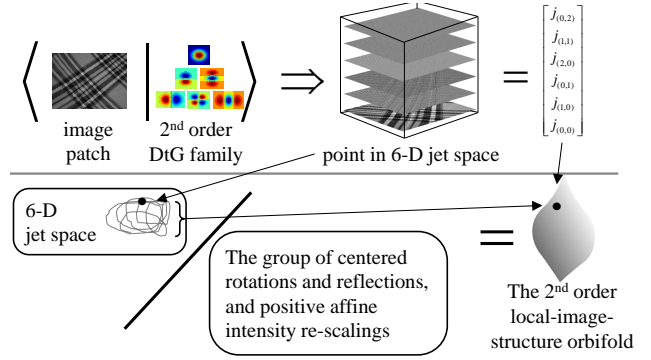


Fig. 2: Diagrammatically, (top-left) the measurement of image structure using a bank of DtG filters up to second order and the resulting jet (top-right).

It is noted that the DtGs are not orthonormal kernel (e.g., $\langle G_\sigma^{(2,0)} | G_\sigma^{(0,2)} \rangle = 1/(16\pi\sigma^6)$) to avoid incorrect presumption. For the structure up to k^{th} order, $\{G_\sigma^{(m,n)} | 0 \leq m+n \leq k\}$, the vector of DtG responses $J_{(m,n)}^k = \langle G_\sigma^{(m,n)} | I \rangle$ is referred to as a local \mathcal{L} -jet, where $J_{(m,n)}^k \in \mathbb{R}^{\mathcal{L}}$, $\mathcal{L} = \frac{(k+2)!}{2 * k!}$ is called an element of jet space [20]. Here, we are only concerned up to 2nd order structure, the measurements of which require a set of six DtG kernels denoted as,

$$\{\vec{G} = (G_\sigma^{(0,0)}, G_\sigma^{(1,0)}, G_\sigma^{(0,1)}, G_\sigma^{(2,0)}, G_\sigma^{(1,1)}, G_\sigma^{(0,2)})\}$$

, henceforth, called the DtG family (shown in Fig. 1(b)). The DtG responses calculated from Eqn. (4) are denoted as $\{\vec{J} = (J_{(0,0)}^s, J_{(1,0)}^s, J_{(0,1)}^s, J_{(2,0)}^s, J_{(1,1)}^s, J_{(0,2)}^s)\}$ is called a 6-jet (shown in Fig. 2 (top-left)). We denote $\vec{J} = \langle \vec{G} | I \rangle$ for the jet crop up from the image response I . Fig. 3 shows an example of image patches whose local structure is dominated by higher orders (up to 2nd order).

III. PROPOSED DESCRIPTOR

Even the original LBP scheme is simple and computationally efficient, the $\text{LBP}_{R,N}$ histogram descriptor has the following limitations for an effortless application,

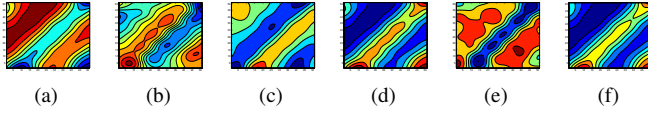


Fig. 3: (a)-(e). Example of different types of local structure upto 2^{nd} order for image patch as shown Fig. 2

- 1) The original $LBP_{R,N}$ produces a larger histogram, 2^N different values, even for small neighborhoods, as shown in Table I in order to reduce its' discriminative power whereas increase storage requirements.
- 2) The original $LBP_{R,N}$ codes are often not robust to image rotation.
- 3) $LBP_{R,N}$ codes are perhaps highly sensitive to noise: the small variation in upper or lower value of the referenced pixel is considered similar to a major contrast.

TABLE I: Dimensions of Different Descriptors

Scale	(R, N)	$LBP_{R,N}$	$LBP_{R,N}^1$	$LBP_{R,N}^2$	$LBP_{R,N}^{2^2}$	CLBP_CSM
1	(1, 8)	256	36	59	10	200
2	(2, 16)	65536	4116	243	18	648
3	(3, 24)	16777216	699252	—	26	1352
4	(4, 32)	2^{32}	large	—	34	2312
5	(5, 40)	2^{40}	large	—	42	3528
1-5		infeasible	infeasible		106	8040

Even the sampling method is similar to that in LBP, this work proposes a new texture descriptor, called local jet pattern (LJP) to overcome the aforementioned problems for classification and to address together 1) invariance to scale, translation, and rotation (or reflection), 2) noise tolerance of a texture image. The texture classification framework using proposed LJP is shown in Fig. 4. The details of the proposed method are as follows.

A. Local Jet Pattern

There is no specific scale at which a real-world natural texture should preferably be used. The hidden feature points are potentially detected by searching image feature locally over all scales. Therefore, it is desirable that the image should be represented in a scale space domain, so that a finite class of resolutions can be considered. In this work, we constructed the local jet pattern (LJP) to analyze the morphology of a texture image using the spatial derivatives of the corresponding image with different isotropic and anisotropic Gaussian structure. Inspired by the working principle of visual cortex system by Florack *et al.* [20], we use here multi-scale \mathcal{L} -jet representation of an image, which is formed using the spatial derivatives. A jet space representation of a texture image is derived from a set of derivative of Gaussian (DtGs) filter responses up to second order, so called local jet vector (LJV), which also satisfies the properties of Scale Space. To obtain LJP, initially, we transform the candidate texture image into local \mathcal{L} -jet ($\mathcal{L} = 6$) using Eqn. (2), where the element of jet represents the responses of the DtGs (discussed in Section-II) upto 2^{nd} order. The scale normalized derivative of 6-jet for a given image I are as follows:

$$\vec{J} = (J_{(0,0)}^s, J_{(1,0)}^s, J_{(0,1)}^s, J_{(2,0)}^s, J_{(1,1)}^s, J_{(0,2)}^s)$$

represented as a vector $\{\vec{J} = (J^1, J^2, \dots, J^{\mathcal{L}-1}, J^{\mathcal{L}})\}$ which we refer to as the local jet vector (LJV) (shown in Fig. 4(b)). The local jet patterns (LJP) are computed after a contrast normalization preprocessing step, motivated by Weber's law [56]. Let $\|J^{(i,j)}\|$ be the ℓ_2 norm of the DtG responses at pixel (i, j) . The normalization of the DtGs responses are computed as,

$$\mathbf{J}^{(i,j)} \leftarrow \mathbf{J}^{(i,j)} \times \frac{\log(1 + \frac{L^{(i,j)}}{0.03})}{L^{(i,j)}}, \quad (5)$$

where $L^{(i,j)} = \|\mathbf{J}^{(i,j)}\|_2$ represents the DtGs response at pixel (i, j) . Finally, the local jet pattern (LJP) for each element in the jet vector for a given center pixel $P_c^{i,j}$ at (i, j) is computed by comparing its gray value $J_c^{i,j}$ with the gray value of a set of N local circularly and equally spaced neighbors $P_{R,N}^{i,j}$ with radius R around the center pixel $P_c^{i,j}$ (Fig. 5). In LJP, a pixel is considered as a center pixel whose all N local neighbors are present within the image in jet space of dimension $M_x \times M_y$. In Fig. 5, $P_{R,N,n}^{i,j}$ having gray value $J_{R,N,n}^{i,j}$ represent n^{th} neighbour of $P_c^{i,j}$ (i.e. n^{th} component of $P_{R,N}^{i,j}$) where n is a positive integer and $n \in [1, N]$. The spatial coordinate (x, y) of $P_{R,N,n}^{i,j}$ with respect to the center, $P_c^{i,j}$ is given as,

$$\begin{aligned} x(P_{R,N,n}^{i,j}) &= i + r(P_{R,N,n}^{i,j}) \times \cos(\theta(P_{R,N,n}^{i,j})) \\ y(P_{R,N,n}^{i,j}) &= j - r(P_{R,N,n}^{i,j}) \times \sin(\theta(P_{R,N,n}^{i,j})) \end{aligned} \quad (6)$$

where $i \in [R+1, M_x - R]$ and $j \in [R+1, M_y - R]$. $r(P_{R,N,n}^{i,j})$ and $\theta(P_{R,N,n}^{i,j})$ denote the polar coordinates of $P_{R,N,n}^{i,j}$ where $n = 1, 2, \dots, N$ and are computed as

$$\begin{aligned} r(P_{R,N,n}^{i,j}) &= R \\ \theta(P_{R,N,n}^{i,j}) &= (n-1) \times \frac{2\pi}{N} \end{aligned} \quad (7)$$

Let $J_c^{i,j,l}$ be a center pixel (i, j) of l^{th} element of jet vector ($l \in [1, \mathcal{L}]$) and $J_{R,N,n}^{i,j,l}$ be the n^{th} neighbor of $J_c^{i,j,l}$ corresponding to the N sampling points with radius R . The array of N neighbors are defined as,

$$\vec{J}_{R,N}^{i,j,l} = [J_{R,N,1}^{i,j,l}, J_{R,N,2}^{i,j,l}, \dots, J_{R,N,N}^{i,j,l}]$$

The LJP response for a given center pixel $J_c^{i,j,l}$ of l^{th} element of local jet vector (LJV) is calculated as,

$$LJP_{R,N}^{i,j,l} = \sum_{n=1}^N 2^{n-1} \times \text{sign}(J_{R,N,n}^{i,j,l} - J_c^{i,j,l}) \quad (8)$$

where sign is a *unit step* function to denote whether a given input is positive or not, and is defined as,

$$\text{sign}(z) = \begin{cases} 1, & z \geq 0 \\ 0, & z < 0 \end{cases}$$

Note that the range of LJP depends on the number of neighboring sampling points (N) around the center $J_{R,N}^{i,j,l}$ and radius R to form the pattern and their values lie between 0 to 2^{N-1} . In other words, the range of LJP is $[0, 2^{N-1}]$. We compute the LJP for all elements of LJV. Fig. 4(c) shows the computed local jet patterns (i.e. $LJP_{R,N}^{i,j,l} | l = 1, 2, \dots, \mathcal{L}$) from each element of LJV (Fig. 4(b)) for a candidate training texture image (Fig. 4(a)).

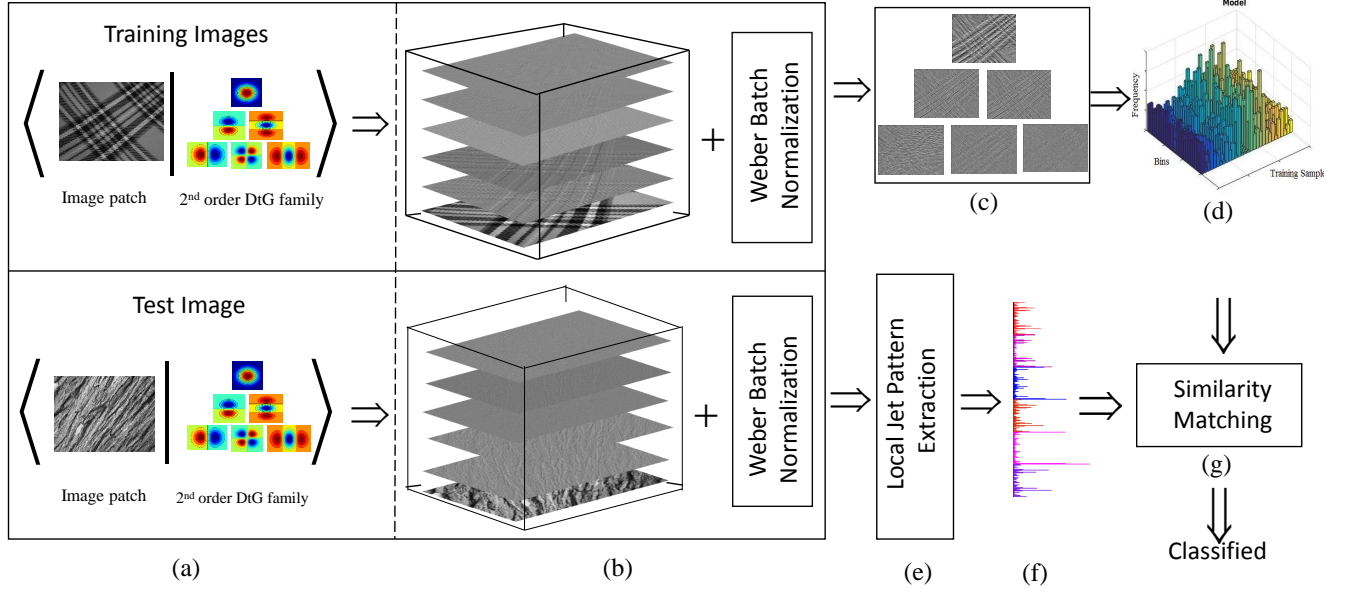


Fig. 4: The texture classification framework using proposed local jet pattern(LJP): (a) texture images with DtGs kernel; (b) the DtGs responses of the texture images (i.e., local jets vector (LJV)); (c) the local jet pattern ($LJP_{R,N}^{i,j,l} | l = 1, 2, \dots, \mathcal{L}$) of individual element of Local Jet Vector (LJV) for a training image; (d) the models of frequency distribution for LJP feature of all training images; (e) extraction of LJP for test image; (f) feature distribution of LJP for test image; (g) similarity matching to classify the test image

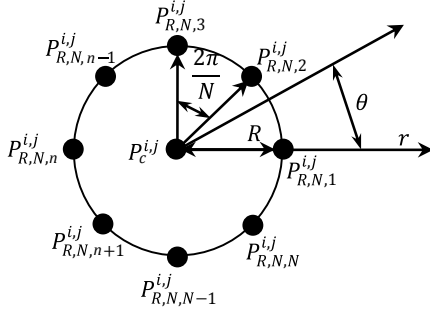


Fig. 5: The local neighbors $P_{R,N,n}^{i,j}$ for ($\forall n \in [1, N]$) of a center pixel $P_c^{i,j}$ in polar coordinate system.

B. LJP Feature Vector

To reduce the classification computation cost using local jet pattern (LJP) of a texture image, we need to compute the frequency of local jet pattern (LJP) for each element of local jet vector (LJV) ($\vec{J} = (J^1, J^2, \dots, J^{\mathcal{L}-1}, J^{\mathcal{L}})$). The frequency of local jet pattern (LJP) (H) of 2^N dimension is calculated for every pixel of LJP image I of size $(M_x \times M_y)$. The normalized LJP histogram feature vector ($\mathbf{H}_{R,N}^{i,j,l}$) for $l^{th} \in [1, \mathcal{L}]$ element of LJV (i.e. $LJP_{R,N}^{i,j,l}$), is computed using the following equation,

$$H_{R,N}^l(\Omega) = \sum_{i=R+1}^{M_x-R} \sum_{j=R+1}^{M_y-R} f(LJP_{R,N}^{i,j,l}(i, j), \Omega) \quad (9)$$

where $\forall \Omega \in [0, 2^N - 1]$ and $f(u, v)$ is a function given by

$$f(u, v) = \begin{cases} 1, & \text{if } u == v \\ 0, & \text{otherwise.} \end{cases}$$

The final LJP feature vector is constructed by concatenating all $H_{R,N}^l$ where $l = 1, 2, \dots, \mathcal{L}$. Since the number of bins in Eqn. (9) of $LJP_{R,N}^{i,j,l}$ for each element of LJV ($l \in [1, \mathcal{L}]$) is 256 when $R = 1, N = 8$. Therefore, the dimension of the LJP feature vector becomes high i.e. $256 \times 6 = 1536$. To cut down the number of bins, we adopted *uniform* pattern scheme [45], which gives 59 bins for each element of LJV and the final normalized LJP feature vector dimension is reduced to $59 \times 6 = 354$. Since the zeroth order terms of DtGs response does not carry any geometrical information, those are discarded. Therefore, the feature vector dimension is further reduced to $59 \times 5 = 295$.

In Appendix. A, we observe that $J_{(0,0)}$ and $J_{(1,1)}$ of LJV are invariant to rotation, or reflex individually. Now, considering LJP for all the elements of LJV, i.e. \mathcal{L} -jet ($\mathcal{L} = 6$) together, is invariant under scale, rotation, or reflation of the image surface. Therefore, the final LJP feature vector is also invariant to scale, rotation, or reflation of the texture image.

We computed and compared the probability distributions of feature vector difference of proposed and state-of-the-art features using sample images of intra and inter class and shown in Fig. 6. The horizontal axis indicates the deviation from zero mean and the vertical axis indicates the probability of feature vector difference for one sample image to another by a particular amount of deviations. The probability at zero mean with high amplitude represents higher similarity between feature vectors whereas larger deviation from zero mean implies the less similarity. Fig. 6 shows that LJP is discriminative as it perfectly differentiates inter class variations (Sample1 and Sample3) and at the same time better matches for intra class images (Sample1 and Sample2).

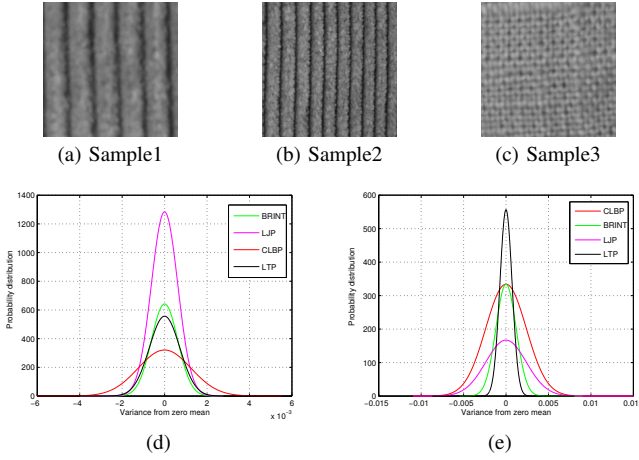


Fig. 6: Illustration of the behavior of LTP, BRINT, CLBP, and LJP for inter and intra class sample images; (a-c) Three texture images taken from KTH-TIPS [25] texture database where Sample1 and Sample2 belong to the same class whereas Sample1 and Sample3 belong to the different classes; (d-e) represents the probability distributions of feature vectors difference with respect to zero mean of different methods for intra and inter class images respectively.

Assuming image of size $M_x \times M_y$ and the kernel of size $P \times Q$, the algorithmic complexity of the proposed descriptors is computed as follows. To create the \mathcal{L} -jet representation of input image in step 4 of Algorithm 1 requires roughly $\mathcal{L}M_xM_yPQ$ multiplications and additions. As 2-D DtGs kernel is separable, filtering is done in two steps. The first step requires about $\mathcal{L}M_xM_yP$ multiplications and additions while the second requires about $\mathcal{L}M_xM_yQ$ multiplications and additions, making a total of $\mathcal{L}M_xM_y(P+Q)$. Since \mathcal{L} and kernel size are constant, the complexity becomes $O(M_xM_y)$. The creation of LJP pattern, as presented in step 11 of Algorithm 1, requires roughly $\mathcal{L}NM_xM_y$ multiplications and additions, and the complexity becomes $O(M_xM_y)$, where N is the number of evenly spaced circular neighbor pixels to each center. As step 13 of Algorithm 1 takes $O(M_xM_y)$ to create histogram of LJP, the time complexity of proposed LJP descriptor is $3M_xM_y \approx O(M_xM_y)$.

C. Comparing Distribution of local Descriptor

To compare distributions of local descriptors, we need to find the distributions of LJPs for training (model) (Fig. 4(d)) and test (sample) images (Fig. 4(f)). A non-parametric statistical test can measure the goodness-of-fit using the dissimilarity of sample and model histograms (Fig. 4(g)). To evaluate the fit between two histograms, there are several metrics such as log-likelihood ratio, histogram intersection, and chi-square (χ^2) statistic [45]. In this work, two non-parametric classifiers is used to analyze the actual classification performance. First, the nearest neighbor classifier (NNC) with the chi-square (χ^2) distance [22] is utilized to evaluate the effectiveness of proposed feature. The comparative distributions of two samples $H_x = x_1, \dots, x_N$ and $H_y = y_1, \dots, y_N$ using the χ^2 distance is defined as,

$$D(H_x, H_y) = \sum_{i=1}^N \frac{(x_i - y_i)^2}{x_i + y_i} \quad (10)$$

Algorithm 1: Algorithm to extract $LJP_{R,N}^{i,j,l}$ descriptor, where N is the number of circular samples taken over circle of radius R .

Data: The texture image (I)

Result: Normalized Local Jet Pattern (HLJP) Descriptor

- 1 initialization ($R = 1, N = 8, k = 2, m = 0, n = 0$);
- 2 **while** ($m \leq 2$ and $n \leq 2$ and $(m + n) \leq 2$) **do**
- 3 Create DtGs Kernel ($G_{\sigma}^{m,n}$) upto $k = 2^{nd}$ Order;
- 4 $J_{(m,n)} = (-1)^{m+n} (G_{\sigma}^{m,n} | I)$;
- 5 **end while**
- 6 $J_{(m,n)}^s = \sigma^{m+n} J_{(m,n)}$
- 7 initialization ($i = R+1, j = R+1, l = 1, \mathcal{L} = \frac{(k+2)!}{2 \times k!}$);
- 8 **while** ($l \leq \mathcal{L}$) **do**
- 9 **while** ($i \leq M_x - R$ and $j \leq M_y - R$) **do**
- 10 $\mathbf{J}^{(i,j,l)} \leftarrow \mathbf{J}^{(i,j,l)} \times \frac{\log(1 + \frac{L^{(i,j)}}{0.03})}{L^{(i,j)}}$;
- 11 $LJP_{R,N}^{(i,j,l)} = \sum_{n=1}^N 2^{(n-1)} \times \text{sign}(J_{R,N,n}^{i,j,l} - J_c^{i,j,l})$;
- 12 **end while**
- 13 $H_{R,N}^l = \text{HIST}(LJP_{R,N}^{i,j,l})$;
- 14 $HLJP = \text{concateNormalizeLJP}(H_{R,N}^l)$;
- 15 **end while**

where N represents the number of bins, H_x and H_y represent the extracted features of a model and a test sample, respectively. The class of test sample H_y is labeled to that class of model that makes smallest χ^2 -distance.

Then another advanced classifier, called nearest subspace classifier NSC [60], is implemented to achieve an improved classification performance. In order to avoid the over emphasizing patterns with large frequency, the proposed feature is preprocessed before fitting to NSC, similar to that in [21]:

$$\bar{X}_k = \sqrt{X_k}, \quad k = 1, 2, \dots, N \quad (11)$$

where N and X_k are the number of bins and the original frequency of the LJP at k^{th} bin, respectively. At first the nearest subspace classifier (NSC) computes the distance of test sample, y to the c^{th} class and calculates the projection residual r_c from y to the orthogonal principle subspace $B_c \in \mathbb{R}^{N \times n}$ of the training sets X_c , which is spanned by the principal eigenvectors of $\Sigma_c = X_c X_c^T$ for the c^{th} class, given as follows,

$$r_c = \|(I - P_{B_c})y\|_2 = \|(I - B_c B_c^T)y\|_2 \quad (12)$$

where $P = I \in \mathbb{R}^{N \times N}$ is a identity matrix where N rows are selected uniformly at random. The test sample y is then assigned to the one of the C classes with the smallest residual among all classes, i.e.

$$i^* = \arg \min_{c=1, \dots, C} r_c \quad (13)$$

IV. EXPERIMENTAL EVALUATION

A. Texture Databases

To evaluate the classification power of the proposed descriptor, a series of experiments is carried out on five large and commonly used texture databases: Outex_TC-00010 (TC10)

[43], Outex_TC-00012 (TC12) [43], Brodatz album [2], KTH-TIPS [25], and CUREt [12] texture databases. The Brodatz database is a well known challenging database to test texture classification algorithms because it contains comparatively large number of texture classes, having the lack of intra-class variation and small number of samples per class. The performance of different methods are evaluated in term of classification accuracy using K-fold cross-validation test along with two non-parametric classifiers, NNC with Chi-Square (χ^2) distance and NSC. In k -fold cross-validation test, the feature set is randomly partitioned into k equal sized subsets ($k = 10$). Out of the k subsets, a single subset is retained as the validation data for testing the classifier, and the remaining ($k - 1$) subsets are used as training data. The average of the classification accuracies over k rounds give us a final cross-validation accuracy. The K-fold cross-validation process provides a more accurate picture of the classification performance. We have normalized each input image to have an average intensity of 128 and a standard deviation of 20 [45]. In VZ-MR8 and VZ-Patch methods, the texture samples are normalized to have an average intensity of 0 and a standard deviation of 1 [54]–[56]. This is done to remove global intensity and contrast. The texture classification accuracies of the proposed descriptor are compared with $LBP_{R,N}$ [45], $LBP_{R,N}^{u2}$, $DLBP_{R,N}$ [34], $LBP_{R,N}^{sri_su2}$ [32], multiscale $CLBP_{R,N}^{sriu2}/M_{R,N}^{riu2}/C(1,8 + 3,16 + 5,24)$ [22] and other state-of-the-art methods. The details of experimental setups are given as follows:

TABLE II: Summary of Texture Database used in Experiment #1

Texture Database	Image Rotation	Illumination Variation	Scale Variation	Texture Classes	Sample Size (pixels)	Samples per Class	Total Samples
Outex_TC10	✓			24	128 x 128	180	4320
Outex_TC12	✓	✓		24	128 x 128	200	4800

EXPERIMENT #1: There are 24 distinct homogeneous texture classes selected from the Outex texture databases [43], each image having the size of 128×128 pixels. **Outex_TC_0-0010 (Outex_TC10)** contains texture images under illuminant “inca” whereas **Outex_TC_00012 (Outex_TC12)** contains texture images with 3 different illuminants (“inca”, “horizon”, and “t184”). Both of the Outex test suit images are collected under 9 different rotation angles (0° , 5° , 10° , 15° , 30° , 45° , 60° , 75° , and 90°) in each texture class. The test suites **Outex_TC_00010 (Outex_TC10)**, and **Outex_TC_00012 (Outex_TC12)** are summarized in Table II.

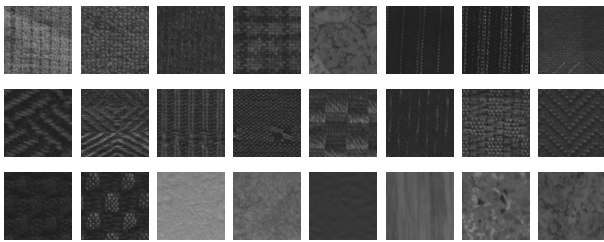


Fig. 7: 24 texture images randomly taken from each class of Outex_TC10 and Outex_TC12 database

EXPERIMENT #2: Brodatz [2] album contains 32 homogeneous texture classes where each image is partitioned into 25 non-overlapping sub-images of size 128×128 , and each sub-image is down-sampled to 64×64 pixels.

TABLE III: Summary of Texture Database used in Experiment #2

Texture Database	Image Rotation	Illumination Variation	Scale Variation	Texture Classes	Sample Size (pixels)	Samples per Class	Total Samples
KTH-TIPS	✓	✓	✓	10	200 x 200	81	810
Brodatz	✓		✓	32	64 x 64	64	2048
CUREt	✓	✓		61	200 x 200	92	5612

CUREt database [12] includes 92 texture images per class and a total of 61 classes. This database is designed to contain large intra-class variation where images are captured under different illuminations and viewing directions with constant scale. All 92 images of 61 texture classes are cropped into 200×200 region and converted to gray scale [55].

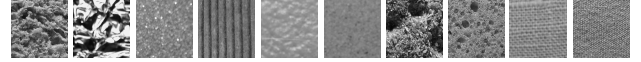


Fig. 8: Ten texture images randomly taken from each class of KTH-TIPS database.

KTH-TIPS database [25] is extended by imaging new samples of ten CUREt textures as shown in Fig. 8. It contains images with 3 different poses, 4 illuminations, and 9 different variations of scales with size 200×200 . The **Brodatz**, **CUREt**, and **KTH-TIPS** databases are summarized in Table III.

B. Results of Experiment #1

The results of Experiment #1, accomplished on Outex_TC10 and Outex_TC12 are tabulated in Table IV. This table includes average classification accuracy of K -fold cross-validation test ($K = 10$) for the proposed descriptor and the comparative summary of the results for $LBP_{(R,N)}$ [45], VZ-MR8 [55], VZ-Patch [56] and recent state-of-the-art methods. We have made the following observations from the results of Experiment #1. Though the feature dimension LBPV and LBP are the same, due to additional contrast measure to the pattern histogram, LBPV produces a significantly better performance compared to the original LBP. $LBP_{R,N}^{riu2}/VAR_{R,N}$ provides better performance compared to $LBP_{R,N}^{riu2}$. This is because LBP and local variance of a texture image are complementary and so, the strength is produced by the joint distribution of LBP and local variance compared to one alone. $CLBP_{R,N}^{sriu2}/M_{R,N}^{riu2}/C(1,8 + 2,16 + 3, 24)$ which is made by fusing the $CLBP_S$ and $CLBP_M/C$, provides better performance compared to other variant of CLBP. This is because it contains complementary features of sign and magnitude, in addition to center pixel.

DLBP + NGF, which makes use of the most frequently occurred 80% patterns of LBP to enhance the classification performance compared to the original $LBP_{R,N}^{u2}$ but like $VAR_{R,N}$ ignores the local spatial structure. In addition, the dimensionality of the DBLP varies with the training samples and it demands a pre-training stage. For comparison, we provide the best results of DLBP with $R = 3$ and $N = 24$ in Table. IV. The state-of-the-art statistical algorithm, VZ-MR8 and VZ-Patch takes dense response from multiple filters. However, the performance is quite low compared to the proposed LJP. In addition, the complexity of feature extraction and matching is quite high [56] compared to the proposed LJP because the MR8 needs to calculate 8 maximum responses after 38 filters

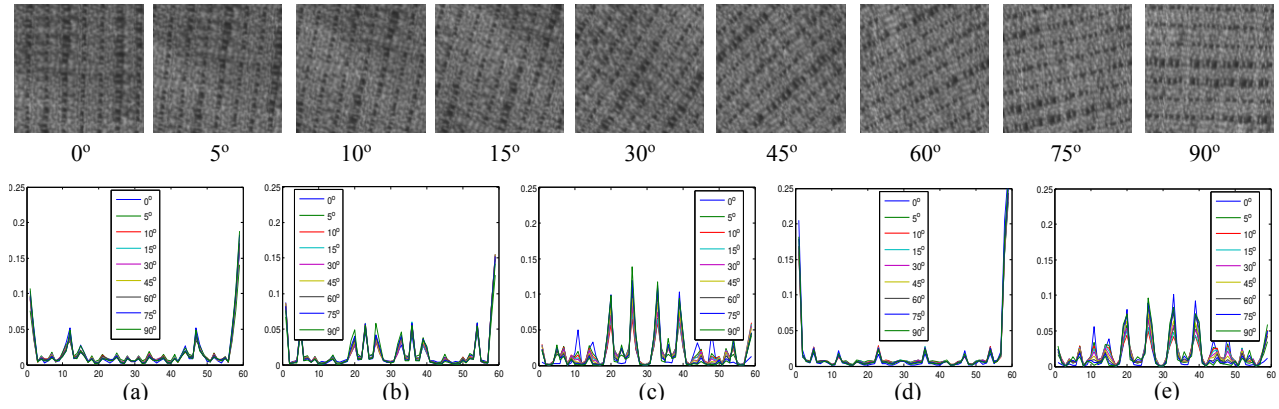


Fig. 9: (a)-(e) represent individual LJP histograms ($H_{R,N}^l | l \in [2, \mathcal{L}]$) of a texture samples are taken from Outex database with 9 different orientations where abscissa and ordinate represent number of bins and feature probability distribution, respectively.

TABLE IV: Average classification accuracy (%) on Outex_TC10 and Outex_TC12 using STATE-OF-THE-ART schemes

Methods	Classifier	Outex_TC10	Outex_TC12		Average
			horizon	t184	
LTP [52]	NNC	76.06	63.42	62.56	67.34
VAR [44]	NNC	90.00	64.35	62.93	72.42
LBP [45]	SVM	97.60	85.30	91.30	91.40
LBP _{R,N}^{riu2}}	NNC	84.89	63.75	65.30	71.31
LBP/VAR	NNC	96.56	78.08	79.31	84.65
LBPV _{R,N}^{riu2}} [23]	NNC	91.56	77.01	76.62	81.73
CLBP_S	NNC	84.81	63.68	65.46	71.31
CLBP_M	NNC	81.74	62.77	59.30	67.93
CLBP_M/C	NNC	90.36	76.66	72.38	79.80
CLBP_S_M/C [22]	NNC	94.53	82.52	81.87	86.30
CLBP_S/M	NNC	94.66	83.14	82.75	86.85
CLBP_S/M/C	NNC	98.93	92.29	90.30	93.84
LBP _{R,N}^{NT}} [19]	NNC	99.24	96.18	94.28	96.56
DLBP _{R=3,N=24} [34]	SVM	98.10	87.40	91.60	92.36
BRINT_CS_CM [38]	NNC	99.35	97.69	98.56	98.53
VZ-MR8 [55]	Nsc	93.59	92.82	92.55	92.99
VZ-Patch [56]	Nsc	92.00	92.06	91.41	91.82
PTP [58]	NNC	99.56	98.08	97.94	98.52
CDCP [50]	NNC	99.76	99.82	99.62	99.72
Proposed LJP	NNC	99.95	99.97	99.81	99.91
Proposed LJP	Nsc	100	99.97	99.88	99.95

convolving with the image and use a clustering technique to build the textons dictionary. The LBP_{R,N}^{NT}} [19] based methods and BRINT [38] give better performance compared to other state-of-the-art LBP methods. However, the accuracies are lower than those obtained by our proposed LJP. This is mainly because LBP_{R,N}^{NT}} extracts features by using locally rotation invariant LBP_{R,N}^{riu2}} approach which produces only 10 bins and such small size of features can not represent each class well, while BRINT extracted large number of features from multiple radius ($R = 1, 2, 3, 4$) by utilizing rotation invariant LBP_{R,N}^{ri}} approach, whereas it loses the global image information.

Finally, even the Outex test suits (Outex_TC10, Outex_TC12 (“horizon” and “t184”)) contain both illuminant and rotation variant of textures the proposed descriptor achieves performance in term of mean accuracy and standard deviations $100 \pm 0.0000\%$, $99.97 \pm 0.0732\%$ and $99.88 \pm 0.1314\%$ on three different suits, respectively. Note that the textures under different illuminant and different viewpoint usually have different micro structures. The comparative results in Table IV shows that the proposed descriptor provides better classification performance compared to other state-of-the-art

methods. The better performance is due to the following attributes. To extract LJP, initially, a jet space representation of a texture image is derived from a set of derivative of Gaussian (DtGs) filter responses up to second order, so called local jet vector (LJV) (Fig. 4). Each element of LJV is encoded via *uniform* pattern scheme which produces 59 bins, are sufficient to discriminate each texture class. All the DtGs responses, LJV together achieve invariance to scale, rotation, or reflection and are able to capture the *micro structure* under different illumination controlled environment (“inca”, “horizon” and “t184”). To visualize the rotation invariant characteristic of the proposed descriptor, an example of LJP feature distribution for a texture samples taken from Outex_TC10 database having 9 different orientations ($0^\circ, 5^\circ, 10^\circ, 15^\circ, 30^\circ, 45^\circ, 60^\circ, 75^\circ$, and 90°) are shown in Fig. 9. Fig 9(a)-(e) represent the histograms ($H_{R,N}^l | l \in [2, \mathcal{L}]$) of individual ($LJP_{R,N}^{i,j,l} | l \in [2, \mathcal{L}]$). It is clearly observed that the LJP feature distribution of different orientations are approximately overlapped which signify the rotation invariance of LJP descriptor.

C. Results of Experiment #2

To analyse the scale invariance property of the proposed approach, we used the KTH-TIPS database which contains images with different scales. Each image of KTH-TIPS is captured in a controlled distance environment [25]. Fig. 10 shows an example texture image having 9 different scales to illustrate the effectiveness of scale invariance properties of LJP descriptor. Fig. 10(S¹)-(S⁹) show nine images of “corduroy” class in KTH-TIPS with different scales. Fig. 10(a)-(e) depict the histograms ($H_{R,N}^l | l \in [2, \mathcal{L}]$) of individual LJP_{R,N}^{i,j,l} descriptor with $R = 1$, and $N = 8$. It is clear from Fig. 10(a)-(e) that the histograms of individual LJP for 9 different scales are approximately closed which imply that the LJP descriptor is scale invariant. The proposed descriptor achieves scale invariance by utilizing the properties of Hermite polynomials. As per Eqn. (1) the details within the Gaussian window is expanded over the basis of Hermite polynomials and this property provides a multi-scale hierarchical image structure for \mathcal{L} -jet although the scale (σ) is fixed [29].}

The average classification accuracy (%) of K -folds cross-validation test ($K = 10$) for the proposed descriptor is shown

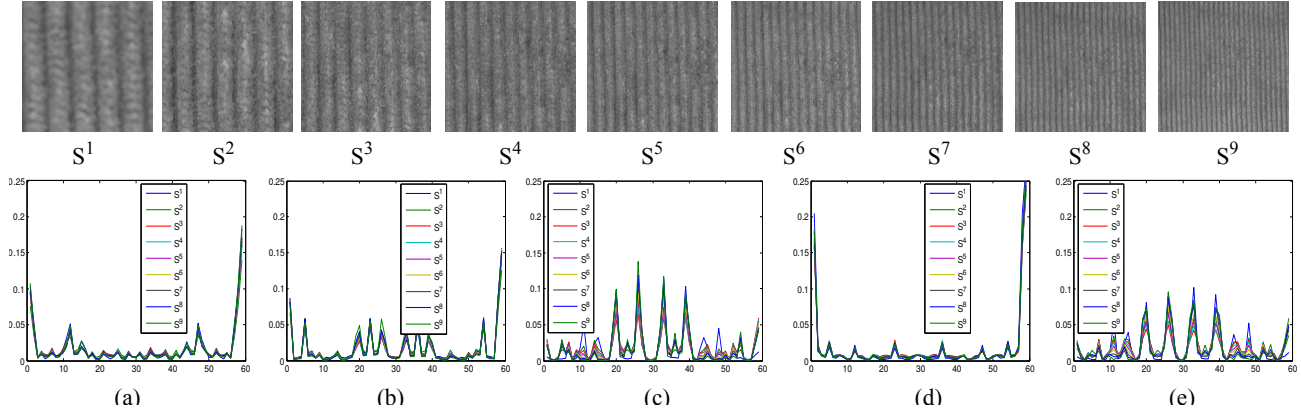


Fig. 10: (a)-(e) represent individual histograms $H_{R,N}^l$ of LJP, where $R=1, N=8$ and $l \in [2, \mathcal{L}]$ of a texture sample are taken from KTH-TIPS [25] database having 9 different scales where abscissa and ordinate represent number of bins and feature probability distribution, respectively.

in Table V. This table also gives a comparative summary of the results for variants of LBP and other state-of-the-art methods on three well known benchmark texture databases (KTH-TIPS, Brodatz, and CURET). The following observations have been noted from Table V. The proposed descriptor gives good performance with simple non-parametric NNC classifier on three commonly used challenging databases. The performance is further improved, when an advanced classifier, NSC is used. The NSC classifier gives much better performance compared to the NNC classifier for the same descriptor because: (i) for a given test sample NSC uses all training samples of the same class while NNC uses one training sample only; (ii) NSC is more robust to outlier and noise as it uses the correlation between different samples. DLBP combining with Gabors feature, attains a higher classification rate than original LBP with NNC. However, its performance is quite less than the proposed LJP. This is mainly because DLBP does not consider scale variation, so it can't provide better performance on complex databases. The scale invariant feature $LBP_{R,N}^{sri-su2}$ provides better performance than $LBP_{R,N}^{riu2}$ where $R=1, 2, 3$ and $N=8, 16, 24$, respectively. However the performance is lower than multi-resolution $LBP_{R,N}^{riu2}$ and $CLBP_{S_{R,N}^{riu2}}/M_{R,N}^{riu2}/C$, and much lesser than the proposed descriptor. This happens because the extraction of consistent and accurate scale for each pixel is difficult. The $LBP_{R(i,j),8}^{sri-su2}$ provides good performance in controlled environment [32], but it fails over more complex databases. Multi-scale BIF [11] at scales $\sigma, 2\sigma, 4\sigma$, and 8σ gives better performance than the proposed LJP with NNC classifier. This is mainly because BIF uses pyramid histogram with time inefficient shift matching scheme. However, the feature dimension of BIF [11] is too large ($6^4 = 1296$) compared to proposed LJP ($59 \times 6 = 354$) and the shift matching scheme is time consuming. The performance of BIF reduces when scale shifting scheme is not considered [11].

Although the images are captured under scale, rotations, and illumination variations, the proposed LJP gives sound performance in term of mean accuracy and standard deviations i.e. $99.75 \pm 0.790\%$, $99.166 \pm 0.4858\%$, and $99.65 \pm 0.45\%$, on KTH-TIPS [25], Brodatz [2], and CURET [12] texture databases [42], respectively. The classification performance

TABLE V: Comparative results of classification accuracy achieved by the proposed and other state-of-the-art methods

Methods	Classifier	Classification Accuracy (%)		
		KTH-TIPS [25]	Brodatz [2]	CURET [12]
VZ-MR8 [55]	NNC	94.50	94.62	97.43
VZ-Patch [56]	NNC	92.40	87.10	98.03
Lazebnik <i>et al.</i> [31]	NNC	91.30	-	72.50
Zhang <i>et al.</i> [70]	SVM	96.10	-	95.30
MFS [63]	NNC	81.62	-	-
PFS [46]	SVM	97.35	-	-
BIF [11]	Shift NNC	98.50	98.47	98.60
BRINT [38]	NNC	97.75	99.22	97.06
LBP_{18}^{riu2} [45]	NNC	82.67	82.16	80.63
$DLBP_{24}^{riu2}$ [34]	SVM	86.99	99.16	84.93
$LBP_{18}^{sri-su2}$ [32]	NNC	89.73	69.50	85.00
$LBP_{(1.8+2.16+3.24)}^{riu2}$ [45]	NNC	95.17	-	95.84
CLBP_SMC [22]	NNC	97.19	-	97.40
SSLBP [21]	NNC	97.80	-	98.55
Proposed LJP	NNC	98.12	97.31	98.12
Proposed LJP	NSC	99.75	99.16	99.65

TABLE VI: One way statistical ANOVA test results for Outex, KTH-TIPS, Brodatz, and CURET databases, where level of significance is selected as $\alpha = 0.05$.

Source	SS	df	MS	F	Prob (p) > F
Groups	2178.22	07	311.175	15.93	$8.28653e^{-09}$
Error	0625.20	32	019.538		
Total	2803.42	39			

results in Table V shows that the proposed descriptor achieves better and comparable performance compared to the state-of-the-art methods. Though the trend is clear from the performance shown in Table IV, we have further analysed the performance using one way statistical Analysis of variance (ANOVA) test [27]. ANOVA is a collection of statistical test used to analyze the differences among group means and their associated procedures. The null hypothesis H_0 for the test indicates that, *there is no significant difference among group means*. We have taken the significant level $\alpha = 0.05$ for this ANOVA test. We can reject H_0 if the p -value for an experiment is less than the selected significant level and which implies that the at least one group mean is significantly different from the others. To understand the performance of the proposed LJP descriptor was significantly differs from well-known descriptors such as VZ-Patch, VZ-MR8, BRINT, DLBP, CLBP, and LBP^{riu2} , we conduct an one way ANOVA

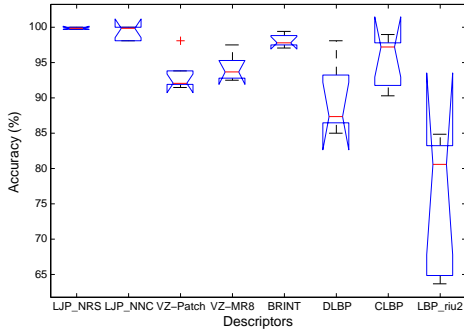


Fig. 11: The box plot (Descriptor vs. Accuracy) corresponding to one way statistical ANOVA test for proposed LJP and state-of-the-art descriptors on Outex, KTH-TIPS, Brodatz, CURET databases.

test with significance level is kept as $\alpha = 0.05$. The test results are shown in Table VI. It is observed from Table VI the p -value ($8.28653e^{-09}$) is less than the pre-select significant level $\alpha = 0.05$ and this indicates that the performance of proposed descriptor significantly differs from other descriptors and hence reject the hypothesis H_0 . In addition, the box plot corresponding to aforementioned ANOVA test is shown in Fig. 11, which also clearly indicates the mean performance of proposed descriptor is significantly better than the well-known descriptors such as VZ-MR8 [55], VZ-Patch [56], BRINT [38], DLBP [34], CLBP [22], and LBP^{riu2} [45].

D. Experiment #3

To study the classification performance of the proposed method in a noisy environment, the experiments are carried out on Outex_TC10 texture database (discussed in subsec. IV-A) incorporating additive white Gaussian noise with different Signal to Noise Ratio (SNR) in dB. Training and testing are done in the same situation as mentioned in noise-free condition. Table VII demonstrates the noise robustness of

TABLE VII: Classification Accuracy (%) of Proposed method and Different STATE-OF-THE-ART methods on **Outex_TC10** with Different Noise Levels in term of dB.

Methods	Classifier	Classification Accuracy (%)				
		SNR = 100	SNR = 30	SNR = 15	SNR = 10	SNR = 5
LBP^{riu2} [45]	NNC	95.03	86.93	67.24	49.79	24.06
$LBP_{R,N,k}^T$ [19]	NNC	-	99.79	99.76	99.76	99.74
CLBP_SMC [22]	NNC	99.30	98.12	94.58	86.07	51.22
$LTP_{R=3,N=24}^{riu2}$ [52]	NNC	99.45	98.31	93.44	84.32	57.37
NRLBP $_{R,N}^{riu2}$ [48]	NNC	84.49	81.16	77.52	70.16	50.88
BRINT [38]	NNC	97.76	96.48	95.47	92.97	88.31
Proposed $LJP_{R,N}^{riu2}$	NNC	99.95	99.83	99.79	99.74	99.74
Proposed $LJP_{R,N}^{riu2}$	Nsc	99.95	99.95	99.95	99.95	99.83

different methods on Outex_TC10 database by comparing the classification rates for different noise levels (measured using SNR i.e Signal to Noise Ratio). The proposed descriptor achieves state-of-the-art results in term of mean accuracy and standard deviations $99.95 \pm 0.0976\%$, $99.95 \pm 0.0976\%$, $99.95 \pm 0.0976\%$, $99.95 \pm 0.0976\%$, and $99.83 \pm 0.0975\%$ on SNR = 100 dB, 30 dB, 15 dB, 10 dB, and 5 dB, respectively. It can be seen that only the proposed LJP method is very modestly improved. This is due to the large smoothing kernels of DtGs which makes it robust to noise. The proposed method has inherited this property from the DtGs in contrast to the LBP and its variants.

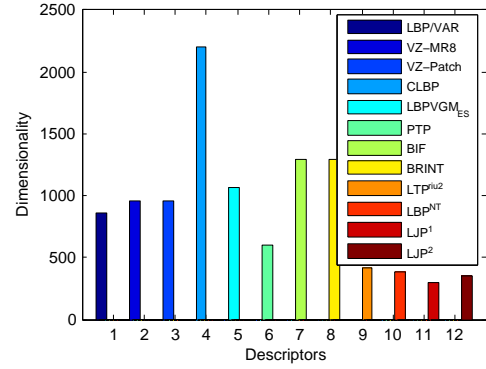


Fig. 12: Comparison of feature dimensionality between proposed and state-of-the-art features.

The dimensionality of the proposed descriptors and other state-of-the-art descriptor are shown in Fig. 12. This figure clearly indicates that the dimensionality of the proposed descriptors (LJP^1 has dimensionality of 295 and LJP^2 has dimensionality 354) are significantly less than the other state-of-the-art methods. We have implemented the algorithm in MATLAB 2011 environment and executed the program on Intel[®] Core[™]2 Duo CPU T6400 @ 2.00GHz \times 2 processors and 3GB RAM with UBUNTU 14.04 LTS operating system. The average feature extraction and matching time cost per-image on four benchmark texture databases by the proposed LJP descriptor are listed in Table VIII. It has been observed that the complexity of the proposed LJP descriptor linearly varies with the image size and the matching complexity also varies linearly with the number of training samples. It shows that the proposed descriptor is fast enough for real time applications.

TABLE VIII: Average feature extraction and matching time of the proposed method.

Time (sec)	Texture Databases				
	KTH-TIPS	Brodatz	CURET	Outex_TC10	Outex_TC12
LJP Feature Extraction	0.22	0.115	0.190	0.119	0.122
Matching using NNC	0.0031	0.0080	0.0228	0.0164	0.0167
Matching using Nsc	0.0109	0.0363	0.1432	0.0810	0.0839

V. CONCLUSIONS

This paper proposes a simple, efficient yet robust descriptor, LJP for texture classification. First, a jet space representation of a texture image is formed by the responses of a set of derivative of Gaussian (DtGs) filter upto 2^{nd} order where DtGs responses preserves the intrinsic local image structure in a hierarchical way by utilizing the properties of Hermite polynomials. Then the local jet patterns (LJP) are computed by comparing the relation between center and neighboring pixels in the jet space. Finally, the histograms of LJP for all elements of jet space representation are concatenated to form the feature vector. The results of the experimental study show that the proposed descriptor delivers quite auspicious performance under scale, rotation, reflection, and illumination variation and fairly robust to the noise. The comparative study indicates the proposed LJP descriptor provides better performance compared to the state-of-the-art methods and in addition, the dimensionality of the final extracted feature

vector is significantly less. While offering reasonably less time to extracts feature with a small feature dimension, the proposed LJP can be applicable in real time scenario.

REFERENCES

- [1] Andrearczyk, V., Whelan, P.F.: Using filter banks in convolutional neural networks for texture classification. *Pattern Recognition Letters* **84**, 63–69 (2016)
- [2] Brodatz, P.: Textures: a photographic album for artists and designers. New York, NY, USA: Dover Pubns (1966)
- [3] Chan, T.H., Jia, K., Gao, S., Lu, J., Zeng, Z., Ma, Y.: Pcanet: A simple deep learning baseline for image classification? *IEEE Transactions on Image Processing* **24**(12), 5017–5032 (2015)
- [4] Chang, X., Ma, Z., Lin, M., Yang, Y., Hauptmann, A.G.: Feature interaction augmented sparse learning for fast kinect motion detection. *IEEE Transactions on Image Processing* **26**(8), 3911–3920 (2017). DOI 10.1109/TIP.2017.2708506
- [5] Chang, X., Ma, Z., Yang, Y., Zeng, Z., Hauptmann, A.G.: Bi-level semantic representation analysis for multimedia event detection. *IEEE Transactions on Cybernetics* **47**(5), 1180–1197 (2017). DOI 10.1109/TCYB.2016.2539546
- [6] Chang, X., Yu, Y.L., Yang, Y., Xing, E.P.: Semantic pooling for complex event analysis in untrimmed videos. *IEEE Transactions on Pattern Analysis and Machine Intelligence* **39**(8), 1617–1632 (2017). DOI 10.1109/TPAMI.2016.2608901
- [7] Chaudhuri, B.B., Sarkar, N.: Texture segmentation using fractal dimension. *IEEE Transactions on Pattern Analysis and Machine Intelligence* **17**(1), 72–77 (1995)
- [8] Chen, J.L., Kundu, A.: Rotation and gray scale transform invariant texture identification using wavelet decomposition and hidden Markov model. *IEEE Transactions on Pattern Analysis and Machine Intelligence* **16**(2), 208–214 (1994)
- [9] Cimpoi, M., Maji, S., Kokkinos, I., Vedaldi, A.: Deep filter banks for texture recognition, description, and segmentation. *International Journal of Computer Vision* **118**(1), 65–94 (2016)
- [10] Cimpoi, M., Maji, S., Vedaldi, A.: Deep filter banks for texture recognition and segmentation. In: *Proceedings of the IEEE Conference on Computer Vision and Pattern Recognition*, pp. 3828–3836 (2015)
- [11] Crosier, M., Griffin, L.D.: Using basic image features for texture classification. *International Journal of Computer Vision* **88**(3), 447–460 (2010)
- [12] Dana, K.J., Van Ginneken, B., Nayar, S.K., Koenderink, J.J.: Reflectance and texture of real-world surfaces. *ACM Transactions On Graphics (TOG)* **18**(1), 1–34 (1999)
- [13] Deng, H., Clausi, D.A.: Gaussian MRF rotation-invariant features for image classification. *IEEE transactions on pattern analysis and machine intelligence* **26**(7), 951–955 (2004)
- [14] Dubey, S.R., Singh, S.K., Singh, R.K.: Rotation and illumination invariant interleaved intensity order-based local descriptor. *IEEE Transactions on Image Processing* **23**(12), 5323–5333 (2014)
- [15] Dubey, S.R., Singh, S.K., Singh, R.K.: Local wavelet pattern: A new feature descriptor for image retrieval in medical ct databases. *IEEE Transactions on Image Processing* **24**(12), 5892–5903 (2015)
- [16] Dubey, S.R., Singh, S.K., Singh, R.K.: A multi-channel based illumination compensation mechanism for brightness invariant image retrieval. *Multimedia Tools and Applications* **74**(24), 11,223–11,253 (2015)
- [17] Dubey, S.R., Singh, S.K., Singh, R.K.: Multichannel decoded local binary patterns for content-based image retrieval. *IEEE Transactions on Image Processing* **25**(9), 4018–4032 (2016)
- [18] Dubey, S.R., Singh, S.K., Singh, R.K.: Local svd based nir face retrieval. *Journal of Visual Communication and Image Representation* **49**, 141–152 (2017)
- [19] Fathi, A., Naghsh-Nilchi, A.R.: Noise tolerant local binary pattern operator for efficient texture analysis. *Pattern Recognition Letters* **33**(9), 1093–1100 (2012)
- [20] Florack, L., Romeny, B.T.H., Viergever, M., Koenderink, J.: The Gaussian scale-space paradigm and the multiscale local jet. *International Journal of Computer Vision* **18**(1), 61–75 (1996)
- [21] Guo, Z., Wang, X., Zhou, J., You, J.: Robust texture image representation by scale selective local binary patterns. *IEEE Transactions on Image Processing* **25**(2), 687–699 (2016)
- [22] Guo, Z., Zhang, L., Zhang, D.: A completed modeling of local binary pattern operator for texture classification. *IEEE Transactions on Image Processing* **19**(6), 1657–1663 (2010)
- [23] Guo, Z., Zhang, L., Zhang, D.: Rotation invariant texture classification using LBP variance (LBPV) with global matching. *Pattern recognition* **43**(3), 706–719 (2010)
- [24] Haralick, R.M., Shanmugam, K., et al.: Textural features for image classification. *IEEE Transactions on systems, man, and cybernetics* (6), 610–621 (1973)
- [25] Hayman, E., Caputo, B., Fritz, M., Eklundh, J.O.: On the significance of real-world conditions for material classification. In: *European conference on computer vision*, pp. 253–266. Springer (2004)
- [26] Heikkilä, M., Pietikäinen, M., Schmid, C.: Description of interest regions with local binary patterns. *Pattern recognition* **42**(3), 425–436 (2009)
- [27] Iversen, G.R., Norpoth, H.: *Analysis of variance*. 1. Sage (1987)
- [28] Kashyap, R.L., Khotanzad, A.: A model-based method for rotation invariant texture classification. *IEEE Transactions on Pattern Analysis and Machine Intelligence* (4), 472–481 (1986)
- [29] Koenderink, J.J., van Doorn, A.J.: Representation of local geometry in the visual system. *Biological cybernetics* **55**(6), 367–375 (1987)
- [30] Krizhevsky, A., Sutskever, I., Hinton, G.E.: Imagenet classification with deep convolutional neural networks. In: *Advances in neural information processing systems*, pp. 1097–1105 (2012)
- [31] Lazebnik, S., Schmid, C., Ponce, J.: A sparse texture representation using local affine regions. *IEEE Transac-*

- tions on Pattern Analysis and Machine Intelligence **27**(8), 1265–1278 (2005)
- [32] Li, Z., Liu, G., Yang, Y., You, J.: Scale-and rotation-invariant local binary pattern using scale-adaptive texon and subuniform-based circular shift. *IEEE Transactions on Image Processing* **21**(4), 2130–2140 (2012)
- [33] Li, Z., Nie, F., Chang, X., Yang, Y.: Beyond trace ratio: Weighted harmonic mean of trace ratios for multiclass discriminant analysis. *IEEE Transactions on Knowledge and Data Engineering* **29**(10), 2100–2110 (2017). DOI 10.1109/TKDE.2017.2728531
- [34] Liao, S., Law, M.W., Chung, A.C.: Dominant local binary patterns for texture classification. *IEEE transactions on image processing* **18**(5), 1107–1118 (2009)
- [35] Lindeberg, T.: Scale-space theory: A basic tool for analyzing structures at different scales. *Journal of applied statistics* **21**(1-2), 225–270 (1994)
- [36] Liu, L., Fieguth, P.: Texture classification from random features. *IEEE Transactions on Pattern Analysis and Machine Intelligence* **34**(3), 574–586 (2012)
- [37] Liu, L., Fieguth, P., Wang, X., Pietikäinen, M., Hu, D.: Evaluation of lbp and deep texture descriptors with a new robustness benchmark. In: *European Conference on Computer Vision*, pp. 69–86. Springer (2016)
- [38] Liu, L., Long, Y., Fieguth, P.W., Lao, S., Zhao, G.: Brint: binary rotation invariant and noise tolerant texture classification. *IEEE Transactions on Image Processing* **23**(7), 3071–3084 (2014)
- [39] Lowe, D.G.: Distinctive image features from scale-invariant keypoints. *International journal of computer vision* **60**(2), 91–110 (2004)
- [40] Mao, J., Jain, A.K.: Texture classification and segmentation using multiresolution simultaneous autoregressive models. *Pattern recognition* **25**(2), 173–188 (1992)
- [41] Martens, J.B.: The hermite transform-theory. *IEEE Transactions on Acoustics, Speech, and Signal Processing* **38**(9), 1595–1606 (1990)
- [42] Mikolajczyk, K., Schmid, C.: A performance evaluation of local descriptors. *IEEE transactions on pattern analysis and machine intelligence* **27**(10), 1615–1630 (2005)
- [43] Ojala, T., Maenpaa, T., Pietikainen, M., Viertola, J., Kyllonen, J., Huovinen, S.: Outex-new framework for empirical evaluation of texture analysis algorithms. In: *Pattern Recognition, 2002. Proceedings. 16th International Conference on*, vol. 1, pp. 701–706. IEEE (2002)
- [44] Ojala, T., Pietikäinen, M., Harwood, D.: A comparative study of texture measures with classification based on featured distributions. *Pattern recognition* **29**(1), 51–59 (1996)
- [45] Ojala, T., Pietikainen, M., Maenpaa, T.: Multiresolution gray-scale and rotation invariant texture classification with local binary patterns. *IEEE Transactions on pattern analysis and machine intelligence* **24**(7), 971–987 (2002)
- [46] Quan, Y., Xu, Y., Sun, Y.: A distinct and compact texture descriptor. *Image and Vision Computing* **32**(4), 250–259 (2014)
- [47] Randen, T., Husoy, J.H.: Filtering for texture classification: A comparative study. *IEEE Transactions on pattern analysis and machine intelligence* **21**(4), 291–310 (1999)
- [48] Ren, J., Jiang, X., Yuan, J.: Noise-resistant local binary pattern with an embedded error-correction mechanism. *IEEE Transactions on Image Processing* **22**(10), 4049–4060 (2013)
- [49] Roy, S.K., Chanda, B., Chaudhuri, B.B., Banerjee, S., Ghosh, D.K., Dubey, S.R.: Local directional zigzag pattern: A rotation invariant descriptor for texture classification. *Pattern Recognition Letters* **108**, 23–30 (2018)
- [50] Roy, S.K., Chanda, B., Chaudhuri, B.B., Ghosh, D.K., Dubey, S.R.: A Complete Dual-Cross Pattern for Unconstrained Texture Classification. In: *Proceedings of the 4th Asian Conference on Pattern Recognition (ACPR 2017)*, Nanjing, China, pp. 741–746. IEEE (2017)
- [51] Roy, S.K., Chanda, B., Chaudhuri, B.B., Ghosh, D.K., Dubey, S.R.: Local morphological pattern: A scale space shape descriptor for texture classification. *Digital Signal Processing, Elsevier (In Press)* (2018)
- [52] Tan, X., Triggs, B.: Enhanced local texture feature sets for face recognition under difficult lighting conditions. In: *International Workshop on Analysis and Modeling of Faces and Gestures*, pp. 168–182. Springer (2007)
- [53] Umer, S., Dhara, B.C., Chanda, B.: A novel cancelable iris recognition system based on feature learning techniques. *Information Sciences* **406**, 102–118 (2017)
- [54] Varma, M., Garg, R.: Locally invariant fractal features for statistical texture classification. In: *Computer Vision, 2007. ICCV 2007. IEEE 11th International Conference on*, pp. 1–8. IEEE (2007)
- [55] Varma, M., Zisserman, A.: A statistical approach to texture classification from single images. *International Journal of Computer Vision* **62**(1-2), 61–81 (2005)
- [56] Varma, M., Zisserman, A.: A statistical approach to material classification using image patch exemplars. *IEEE transactions on pattern analysis and machine intelligence* **31**(11), 2032–2047 (2009)
- [57] Victor, J.D., Knight, B.W.: Simultaneously band and space limited functions in two dimensions, and receptive fields of visual neurons. In: *Perspectives and Problems in Nonlinear Science*, pp. 375–419. Springer (1994)
- [58] Wang, K., Bichot, C.E., Zhu, C., Li, B.: Pixel to patch sampling structure and local neighboring intensity relationship patterns for texture classification. *IEEE Signal Processing Letters* **20**(9), 853–856 (2013)
- [59] WEISS, I.: Geometric invariants and object recognition. *International journal of computer vision* **10**(3), 207–231 (1993)
- [60] Wright, J., Yang, A.Y., Ganesh, A., Sastry, S.S., Ma, Y.: Robust face recognition via sparse representation. *IEEE transactions on pattern analysis and machine intelligence* **31**(2), 210–227 (2009)
- [61] Xie, L., Zhu, L., Chen, G.: Unsupervised multi-graph cross-modal hashing for large-scale multimedia retrieval. *Multimedia Tools and Applications* **75**(15), 9185–9204 (2016)
- [62] Xie, X., Mirmehdi, M.: A Galaxy of Texture Features. In: *Handbook Of Texture Analysis*, pp. 375–406. World Scientific (2008)

- [63] Xu, Y., Ji, H., Fermüller, C.: A projective invariant for textures. In: Computer Vision and Pattern Recognition, 2006 IEEE Computer Society Conference on, vol. 2, pp. 1932–1939. IEEE (2006)
- [64] Xu, Y., Ji, H., Fermüller, C.: Viewpoint invariant texture description using fractal analysis. *International Journal of Computer Vision* **83**(1), 85–100 (2009)
- [65] Yao, C.H., Chen, S.Y.: Retrieval of translated, rotated and scaled color textures. *Pattern Recognition* **36**(4), 913–929 (2003)
- [66] Young, R.A., Lesperance, R.M., Meyer, W.W.: The gaussian derivative model for spatial-temporal vision: I. cortical model. *Spatial vision* **14**(3), 261–319 (2001)
- [67] Zand, M., Doraisamy, S., Halin, A.A., Mustaffa, M.R.: Texture classification and discrimination for region-based image retrieval. *Journal of Visual Communication and Image Representation* **26**, 305–316 (2015)
- [68] Zhang, B., Gao, Y., Zhao, S., Liu, J.: Local derivative pattern versus local binary pattern: face recognition with high-order local pattern descriptor. *IEEE transactions on image processing* **19**(2), 533–544 (2010)
- [69] Zhang, J., Liang, J., Zhao, H.: Local energy pattern for texture classification using self-adaptive quantization thresholds. *IEEE transactions on image processing* **22**(1), 31–42 (2013)
- [70] Zhang, J., Marszałek, M., Lazebnik, S., Schmid, C.: Local features and kernels for classification of texture and object categories: A comprehensive study. *International journal of computer vision* **73**(2), 213–238 (2007)
- [71] Zhu, L., Jin, H., Zheng, R., Feng, X.: Weighting scheme for image retrieval based on bag-of-visual-words. *IET Image Processing* **8**(9), 509–518 (2014)
- [72] Zhu, L., Shen, J., Liu, X., Xie, L., Nie, L.: Learning compact visual representation with canonical views for robust mobile landmark search. *International Joint Conferences on Artificial Intelligence* (2016)
- [73] Zhu, L., Shen, J., Xie, L.: Topic hypergraph hashing for mobile image retrieval. In: *Proceedings of the 23rd ACM international conference on Multimedia*, pp. 843–846. ACM (2015)

Rotation of a surface is a more difficult problem in image analysis. Consider the rotation effect on jet about the origin with an angle θ . Here the zero order derivative term of the jet ($J_{(0,0)}$) remains unaffected. The first order derivative terms are transformed as follows,

$$\begin{pmatrix} J_{(1,0)} \\ J_{(0,1)} \end{pmatrix} \rightarrow \begin{pmatrix} \cos \theta & \sin \theta \\ -\sin \theta & \cos \theta \end{pmatrix} \begin{pmatrix} J_{(0,1)} \\ J_{(1,0)} \end{pmatrix}$$

and the second order terms are transformed according to

$$\begin{pmatrix} J_{(2,0)} \\ J_{(1,1)} \\ J_{(0,2)} \end{pmatrix} \rightarrow \frac{1}{2} \begin{pmatrix} 1+b & 2c & 1-b \\ -c & 2b & c \\ 1-b & -2c & 1+b \end{pmatrix} \begin{pmatrix} J_{(0,2)} \\ J_{(1,1)} \\ J_{(2,0)} \end{pmatrix}$$

where $b = \cos 2\theta$ and $c = \sin 2\theta$. So, to return the starting values, the first order derivative structure requires a full 2π rotation, while the second order derivative structure returns after a rotation by π .

In case of reflection (i.e. the effect of jet about the line $y = x$), the zero order term of the jet is not affected. However, the first order derivative term is transformed according to, $J_{(1,0)} \leftrightarrow J_{(0,1)}$ and the second order derivative term, according to $J_{(2,0)} \leftrightarrow J_{(0,2)}$. Considering all the DtGs responses together, the \mathcal{L} -jet ($\mathcal{L} = 6$) achieves invariance to scale, rotation, or reflection.

Image structure analysis may be appropriate if it considers that intensities are non-negative unconstrained real numbers, and also do not exceed a maximum value. Therefore, the image structure should not be affected by adding a constant (α) to all intensities as in case of uniform illumination change. When such changes arise, only the zero order derivative term is affected and it simply transforms according to, $J_{(0,0)} \rightarrow J_{(0,0)} + \alpha$.

It is also required that the image local structure should be invariant to the multiplication by a non-zero positive factor ($\epsilon > 0$) with all image intensities. In this case, the factor is simply multiplied with all terms of jet vector i.e, $\vec{J} \rightarrow \epsilon \vec{J}$. Note that, it does not require multiplication of intensities by a negative factor to make it invariant to physical constrains.

APPENDIX A

EFFECTS OF SIMILARITY TRANSFORMS

In computer vision problems, a group of transforms are typically chosen to analyse the effect of geometrical structure those are invariant with respect to scaling, translation, rotation and reflection of an image, a constant intensity addition, and multiplication of image intensity by a positive factor and their combinations. In order to cope with the translation effect, we choose the analyzing point as the origin of the co-ordinate system.

In the jet space, Gaussian derivatives are represented by *Hermite* polynomials multiplied with Gaussian window (in Eqn. (1)). The details within the window is expanded over the basis of Hermite polynomials, therefore even if the scale (σ) is fixed, it provides a multi-scale hierarchical image structure for \mathcal{L} -jet [29]